Journal of Photochemistry & Photobiology, A: Chemistry 440 (2023) 114657

Contents lists available at ScienceDirect

Journal of Photochemistry & Photobiology, A: Chemistry

journal homepage: www.elsevier.com/locate/jphotochem

# Design of novel metal chalcogenide photoanodes supported with reduced graphene oxide for improvement of photoelectrochemical hydrogen evolution

Özlem Uğuz Neli [a], Özlem Budak [a], Fatma Karaca [a], Bahadır Keskin [b], Ali Rıza Özkaya [c], Atıf Koca [a,*]

[a] Department of Chemical Engineering, Faculty of Engineering, Marmara University, Maltepe, Istanbul 34854, Turkey
[b] Department of Chemistry, Faculty of Science and Letters, Yıldız Technical University, Esenler, Istanbul 34220, Turkey
[c] Department of Chemistry, Faculty of Science and Letters, Marmara University, Kadıköy, Istanbul 34722, Turkey

ARTICLE INFO

*Keywords:*
Electrodeposition
Quaternary metal chalcogenide thin films
Reduced graphene oxide
Photoelectrochemical performance

ABSTRACT

Designing new photoanodes with high efficiency provides an effective route to develop photoelectrochemical hydrogen production. In this work, quaternary metal chalcogenides (CdZnMSSe (M: Ni, Cu, Mo)) and reduced graphene oxide- quaternary metal chalcogenide (RGO-CdZnMSSe) composite films are fabricated by simple one-step electrodeposition process. The photoanodes formed of quaternary metal chalcogenides and the incorporation of RGO in these composite films increase charge transfer capability and separation ability compared to cadmium-based photoanodes, leading to enhancement of the photoelectrochemical hydrogen production activity. A superior photocurrent response is recorded for RGO(0.25)-$Cd_{0.8}Zn_{0.2}Ni_{0.2}S_{0.2}Se_{0.8}$ (5.34 mA $cm^{-2}$ at 0.8 V vs RHE). In addition, the maximum ABPE value of RGO(0.25)-$Cd_{0.8}Zn_{0.2}Ni_{0.2}S_{0.2}Se_{0.8}$ is determined as 1.95%. The achieved results offer a new insight into highly efficient next generation-photoanodes to convert solar energy to hydrogen.

## 1. Introduction

Growing energy consumption and the resulting impact on the environment necessitate the search for clean and environmentally friendly energy alternatives. Solar energy, as a sustainable energy source, has the great potential to overcome these issues [1]. Harnessing solar energy to generate hydrogen can be opted for because of its low greenhouse gas emissions and high energy density to address global energy and environmental challenges [2].

In this regard, the photoelectrochemical (PEC) system has received a great deal of attention in recent years [3]. This system is based on the coupling of semiconducting light absorbers and electrocatalysts to generate hydrogen. Thus, it has been regarded as a significant step toward sustainable energy supplies. The development of novel high-performance photoelectrodes to capture and convert solar energy to hydrogen is a critical asset in PEC analyses. In this asset, these photoelectrodes need to have the characteristics of well-matched photo absorption with the solar spectrum, efficient photoexcited charge separation to prevent electron-hole recombination, and low photocorrosion rate under light illumination, which are considered the key parameters to the success of solar energy conversion [4,5].

In the last decades, various strategies have been employed to enhance the absorption range of photoelectrodes from UV to visible light. Narrow band gap having semiconductors such as CdSe, CdS, $NiS_x$, $NiSe_x$, $MoS_x$, $MoSe_x$, $CuS_x$, and $CuSe_x$ have the ability to harvest a large portion of the solar spectrum. However, these semiconductors are far from satisfactory due to their poor photostability and high corrosion rate [6]. To report an outstanding photoelectrochemical performance, narrow band gap semiconductors can be integrated with larger band gap semiconductors (i.e., ZnS and ZnSe) to increase the lifetime of photogenerated charge carriers [7]. Furthermore, decorating semiconductors with reduced graphene oxide (RGO) not only improves conductivity but also provides a large specific surface area and increases the charge carrier mobility [8]. Ghasemi and Amiri studied the photoelectrochemical performance of annealed GO/$MoS_2$ and RGO/$MoS_2$ heterostructures and they reported the photocurrent densities of RGO/$MoS_2$ and GO/$MoS_2$ as 0.88 and 0.51 mA $cm^{-2}$, respectively [999999999]. Similarly, Shen et al. investigated the dual effect of RGO

* Corresponding author.
*E-mail address:* akoca@marmara.edu.tr (A. Koca).

https://doi.org/10.1016/j.jphotochem.2023.114657
Received 19 December 2022; Received in revised form 24 February 2023; Accepted 28 February 2023
Available online 5 March 2023

in $TiO_2$/CdSe heterojunction in photoelectrochemical analyses and they concluded that RGO increases the charge separation efficiency and decreases the $e^- - h^+$ recombination rate to a large extent [10]. Because of these, the ability to overcome the limitations that stand in the way of greater photoelectrochemical activity by designing quaternary CdZnMSSe (M: Ni, Cu, Mo) photoelectrodes is advantageous. In contrast to their binary and ternary counterparts, quaternary photoelectrodes enable increased light response capacity, superior $e^- - h^+$ charge carrier mobility, and tuning band-gap alteration by introducing alternative component elements with adjustable stoichiometry. Some reports from the literature verify the improved photoelectrochemical activity of quaternary photoelectrodes [11–14].

To fabricate efficient and stable photoanodes, it is also vital to rationally integrate the semiconductive materials onto the substrate and hence the thin film fabrication methods are quite critical for photoelectrochemical systems. Co-electrodeposition (Co-ED) with repetitive cyclic voltammetry technique (rCV) is a facile, time-saving, economical, easily scalable method allowing to synthesize thin films having good uniformity and strong adherence to the substrate [15]. In the literature, numerous reports are confirming the superiority of the electrodeposition technique over other deposition methods such as hydrothermal, co-precipitation, drop-casting, and film-coating for transition metal chalcogenide photoelectrodes [16–20]. However, the literature is saturated with reports related to the investigation of the PEC performance of binary and ternary transition metal chalcogenides. Herein, we have fabricated a quaternary CdZnMSeS (M: Ni, Cu, Mo) thin film on indium tin oxide (ITO) substrate as a highly efficient photoanode for photoelectrochemical hydrogen production using co-electrodeposition with repetitive cyclic voltammetry technique in a three-electrode set-up, which is presented for the first time. The compositions of RGO, Cd, Zn, S, and Se in RGO-CdZnMSeS composites were determined based on the photoelectrode yielding the highest photocurrent density given in our previous report [17]. The photoelectrochemical analyses of photoelectrodes were performed in aqueous 0.35 mol $dm^{-3}$ $Na_2S$/0.25 mol $dm^{-3}$ $Na_2SO_3$ sacrificial electrolyte (pH = 13.0) under 100 mW $cm^{-2}$ illumination intensity (AM 1.5G). The photoelectrochemical behavior of each photoelectrode was compared and discussed by enlightening their PEC mechanism in terms of their morphology, crystallographic structure, band gap, positions of conduction, and valance bands. Owing to the preventing charge recombination, improving the light absorption ability, and increasing the conductivity through RGO, a novel composite photoanode material for PEC systems is developed with high performance, suggesting an encouraging route in practical applications.

## 2. Experimental

The materials and equipment used in electrodeposition and photoelectrochemical measurements are presented in the Supplementary Information.

### 2.1. Electrodeposition of $Cd_{0.6}Zn_{0.2}M_{0.2}S_{0.2}Se_{0.8}$ (M: Ni, Cu, Mo) and RGO(0.25)-$Cd_{0.8}Zn_{0.2}MS_{0.2}Se_{0.8}$ composite thin films

$Cd_{0.6}Zn_{0.2}MS_{0.2}Se_{0.8}$ (M: Ni, Cu, Mo) and RGO(0.25)-$Cd_{0.8}Zn_{0.2}M_{0.2}S_{0.2}Se_{0.8}$ composite thin films are grown from an aqueous solution of $Cd(CH_3COO)_2{\cdot}2H_2O$, $Zn(CH_3COO)_2{\cdot}2H_2O$, $Ni(NO_3)2{\cdot}.6H_2O$, $Cu(CH_3COO)_2$, $Na_2MoO_4{\cdot}2H_2O$, $Na_2S_2O_3$, $Na_2SeSO_3$ and EDTA. The pH of the solution is adjusted using NaOH. Here, $Na_2SeSO_3$ solution is formed from the dispersion of $Na_2SO_3$ and Se powder in ultrapure water at 80 °C for 4 h. Three electrode electrodeposition technique has been performed for depositing the semiconductor materials on ITO substrates. Pt wire, Ag/AgCl, and ITO substrate are used as a counter electrode, reference electrode, and working electrode, respectively. Before electrodeposition, the substrates are cut into 1 cm × 0.8 cm dimensions and rinsed thoroughly with deionized water and ethanol after cleaning with detergent. The repetitive cyclic voltammetry as an electrodeposition method is applied at the scan rate of 100 mV $s^{-1}$ within the potential range of −1.7 – 1.0 V vs. Ag/AgCl at room temperature. The obtained photoelectrodes are annealed in a horizontal tube furnace at 350 °C for 1 h under an Ar atmosphere. The highest performance is achieved for $Cd_{0.6}Zn_{0.2}Ni_{0.2}S_{0.2}Se_{0.8}$ photoelectrode; therefore, RGO (0.25 mg/ml in the precursor solution based on our previous work) is added in the film structure to improve the photoelectrochemical properties [17]. GO powder has been synthesized in our previous work and the production procedure is given in Supplementary Information in detail [21].

## 3. Results and discussion

Fig. 1 shows the CV curves for the fabrication of CdS, CdSe, ZnS, ZnSe, NiS, NiSe, CuS, CuSe, NiS, NiSe, $MoS_2$, and $MoSe_2$ thin films separately. The aqueous electrolytic bath involves the precursor salt solutions ($Cd(CH_3COO)_2{\cdot}2H_2O$, $Zn(CH_3COO)_2{\cdot}2H_2O$, $Cu(CH_3COO)_2$, $Na_2MoO_4{\cdot}2H_2O$, $Ni(NO_3)_2{\cdot}6H_2O$, $Na_2S_2O_3$,$Na_2SeSO_3$) and EDTA as complexing agent. The pH of the electrolytic bath is adjusted to 8.7 with NaOH. The CV analyses have been performed at 100 mV $s^{-1}$ scan rate. The CV curve for CdS formation on ITO exhibits two cathodic peaks at-1.1 V and-1.3 V vs. Ag/AgCl, and two anodic peaks at -1.1 V and −0.7 V vs. Ag/AgCl corresponding to the reduction of $[Cd\text{-}EDTA]^{2-}$ complexes, reduction of $S_2O_3^{2-}$, oxidation of $S_2O_3^{2-}$, and oxidation and dissolution of Cd. The CV curve for CdSe gives two cathodic peaks and one anodic peak, located at ca. − 1.1 V, −1.3 V, −0.7 V vs. Ag/AgCl. These peaks are ascribed to the reduction of $Cd^{2+}$ ions from $[Cd\text{-}EDTA]^{2-}$ complexes, reduction of selenosulfate ions, and anodic dissolution of CdSe, respectively. ZnS and NiS formation curves display similar patterns to CdS, while the peaks attributed to the ZnSe and NiSe thin film construction are observed in a similar potential range to CdSe. The difference in the CV voltammogram of CuS from other S-containing compounds may be explained by the existence of two stripping anodic peaks at positive potential limits related to the oxidation of copper compounds [22]. Levinas et al. electrodeposited $MoS_2$ thin films on a foam-based photoelectrode and the behavior of the cyclic voltammetric electrodeposition of $MoS_2$ thin film was quite similar to the one we have obtained in our CV voltammogram [23].

Fig. 2 represents the repetitive cyclic voltammetry (rCV) curves for $Cd_{0.6}Zn_{0.2}Mo_{0.2}S_{0.2}Se_{0.8}$ (Fig. 2a), $Cd_{0.6}Zn_{0.2}Cu_{0.2}S_{0.2}Se_{0.8}$ (Fig. 2b), $Cd_{0.6}Zn_{0.2}Ni_{0.2}S_{0.2}Se_{0.8}$ (Fig. 2c), and RGO(0.25)- $Cd_{0.6}Zn_{0.2}Ni_{0.2}S_{0.2}Se_{0.8}$ (Fig. 2d), thin films. The CV curves given in Fig. 2a – c display the characteristic peaks of CdS, CdSe, ZnS, ZnSe, NiS, NiSe, CuS, CuSe, $MoS_2$, and $MoSe_2$. However, the composition of the thin films causes some peaks to become more distinct than others.

### 3.1. Structural analyses of thin films

The field emission scanning electron microscopy (FESEM) images of $Cd_{0.6}Zn_{0.2}Ni_{0.2}S_{0.2}Se_{0.8}$ and RGO(0.25)-$Cd_{0.6}Zn_{0.2}Ni_{0.2}S_{0.2}Se_{0.8}$ are presented in Fig. 3a and b with a magnification of 200000x. It is detected that the RGO sheets are in the CdZnNiSSe particles. Thus, the RGO sheets act as bridges for the connection between different CdZnNiSSe particles, improving the photoelectrochemical performance through the efficient separation of photogenerated carriers. The energy dispersive X-ray spectrometer (EDS) result reveals that the peaks corresponding to Cd, Zn, Ni, S, Se, O, and C elements verify the targeted composition of the related structure on the surface of ITO (Fig. 3c). The signals of Cd, Zn, Ni, S, and Se originate from the CdZnNiSSe particles and the signals coming from C and O elements indicate the existence of RGO in the structure which is also confirmed by the Raman spectrum. The detected In and Si peaks in EDS analyses are attributed to the ITO-coated glass substrate. In addition, the FESEM images which are magnified at 5000x for $Cd_{0.6}Zn_{0.2}Ni_{0.2}S_{0.2}Se_{0.8}$, $Cd_{0.6}Zn_{0.2}Cu_{0.2}S_{0.2}Se_{0.8}$, $Cd_{0.6}Zn_{0.2}Mo_{0.2}S_{0.2}Se_{0.8}$, and RGO(0.25)-$Cd_{0.6}Zn_{0.2}Ni_{0.2}S_{0.2}Se_{0.8}$ are further given in Fig.S1. According to Fig.S1, the more uniform surface is achieved with the presence of RGO in the RGO(0.25)-$Cd_{0.6}Zn_{0.2}Ni_{0.2}S_{0.2}Se_{0.8}$

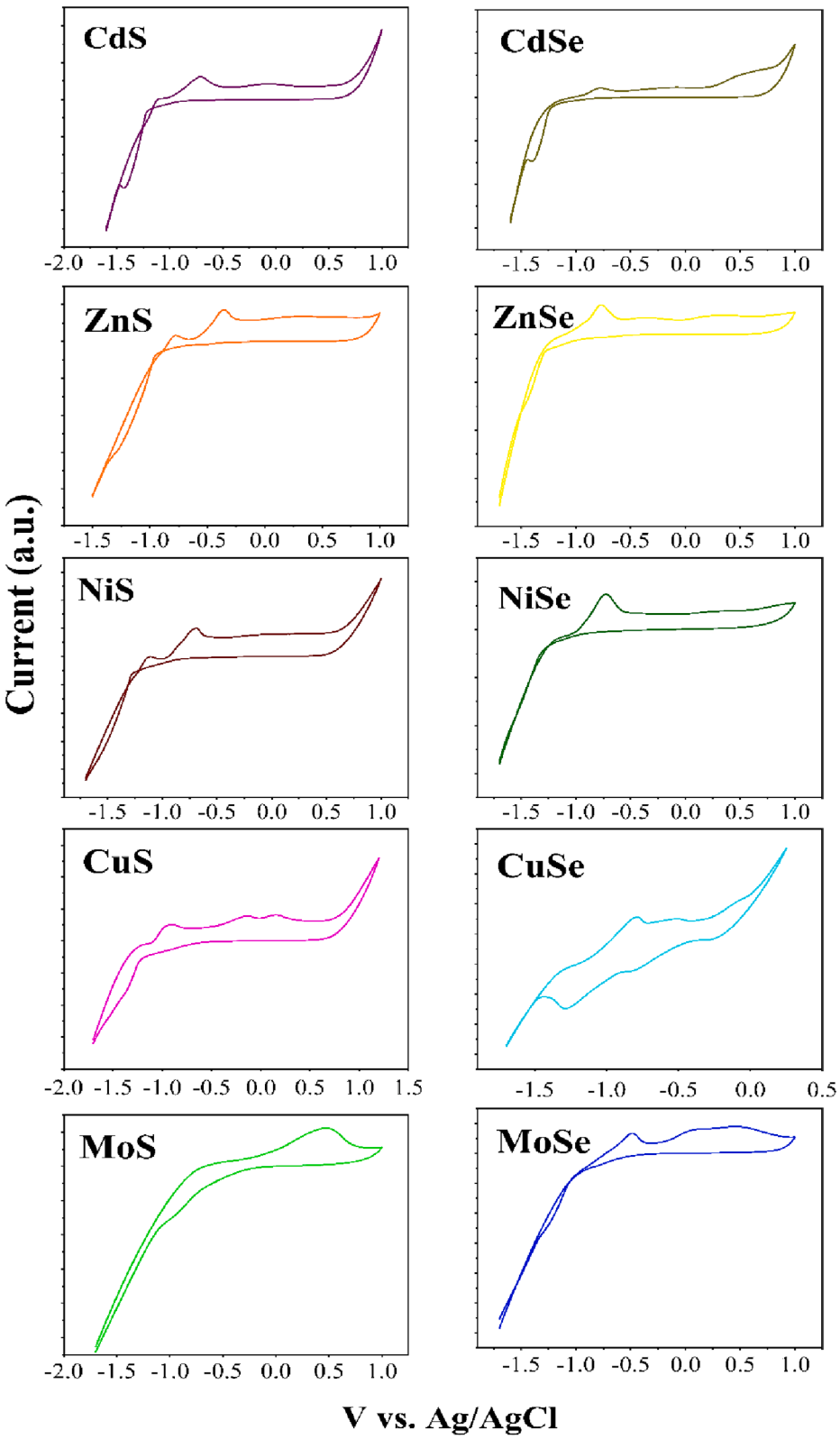


**Fig. 1.** CV curves for the fabrication of CdS, CdSe, ZnS, ZnSe, CuS, CuSe, $MoS_2$, and $MoSe_2$ thin films.

photoelectrode compared to the other fabricated photoelectrodes. Furthermore, the agglomeration of particles on the surface of $Cd_{0.6}Zn_{0.2}Ni_{0.2}S_{0.2}Se_{0.8}$ photoelectrode is relatively less than $Cd_{0.6}Zn_{0.2}Cu_{0.2}S_{0.2}Se_{0.8}$ and $Cd_{0.6}Zn_{0.2}Mo_{0.2}S_{0.2}Se_{0.8}$, leading to the enhancement of the photoelectrochemical activity.

The oxidation states and chemical composition of RGO(0.25)-$Cd_{0.6}Zn_{0.2}Ni_{0.2}S_{0.2}Se_{0.8}$ photoelectrode are typically analyzed by performing XPS (Fig. 4). The survey spectrum confirms the existence of Cd 3d, Zn 2p, Ni 2p, S 2p, Se 3d, O 1 s oxidation states. Each element in XPS is deconvoluted into peaks by Gaussian fitting by using Origin software. The XPS spectrum of $Cd_{0.6}Zn_{0.2}Ni_{0.2}S_{0.2}Se_{0.8}$ is represented in Fig.S2. The characteristic C 1 s peak observed at 284.4 eV on the survey

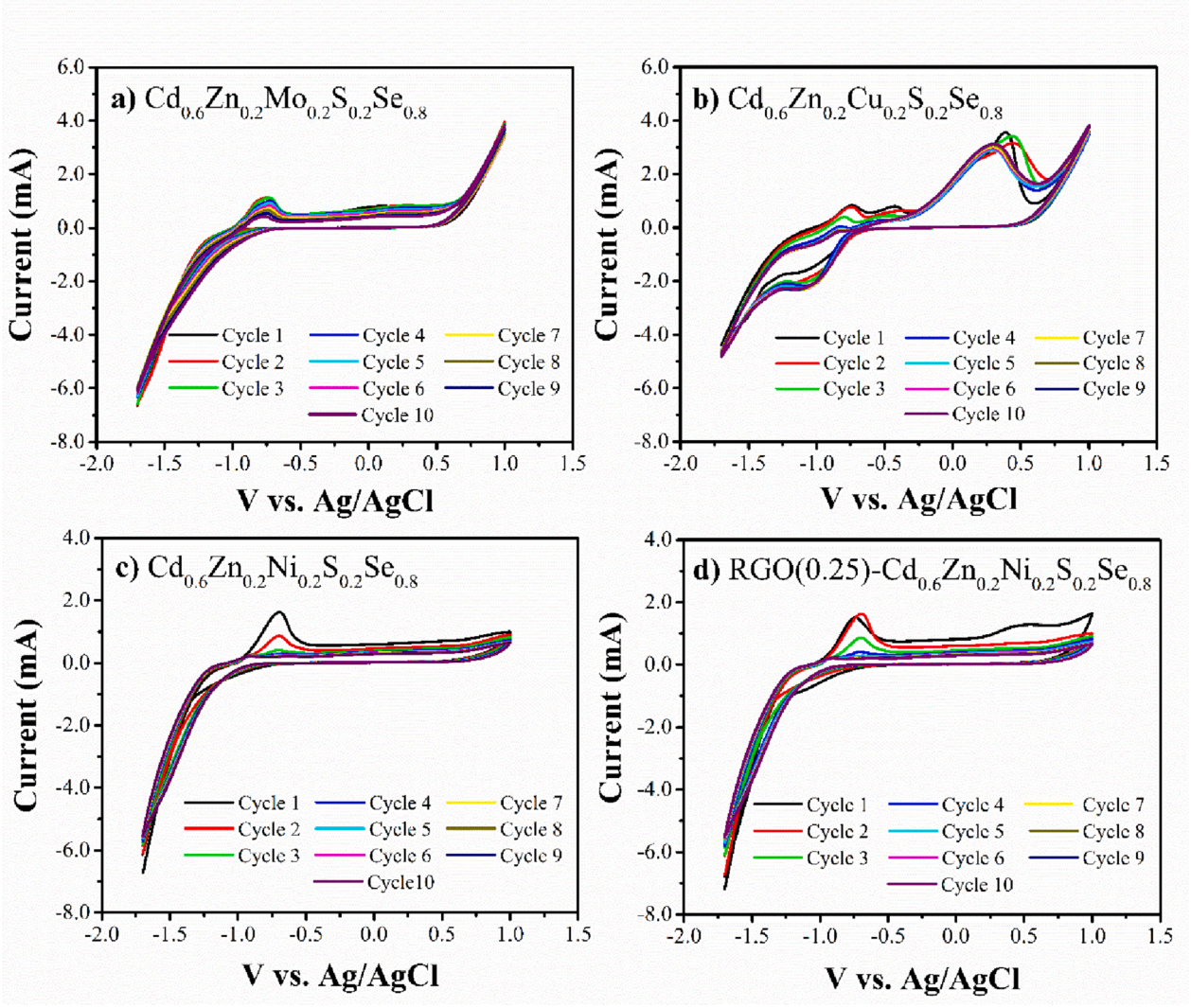


**Fig. 2.** rCv profiles of a) $cd_{0.6}Zn_{0.2}Mo_{0.2}S_{0.2}Se_{0.8}$, b) $Cd_{0.6}Zn_{0.2}Cu_{0.2}S_{0.2}Se_{0.8}$, c) $Cd_{0.6}Zn_{0.2}Ni_{0.2}S_{0.2}Se_{0.8}$, d) RGO(0.25)-$Cd_{0.6}Zn_{0.2}Ni_{0.2}S_{0.2}Se_{0.8}$ composite thin films.

spectrum is used as the reference peak [24].

In Fig. 4, the peaks of Cd 3d are located at 405.5 eV ($3d_{5/2}$) and 412.2 eV ($3d_{3/2}$). The XPS spectrum of Zn 2p reveals the binding energies at 1024 eV ($2p_{3/2}$) and 1047 eV ($2p_{1/2}$) impaired with a satellite peak. The presence of Ni 2p is testified in the XPS spectrum. The two typical peaks centered at around 855.7 eV and 874.6 eV are assigned to the $2p_{3/2}$ and $2p_{1/2}$ oxidation states with their two satellite peaks [25]. S 2p spectrum is divided into two peaks at 160.6 eV and 163.0 eV, corresponding to the $2p_{3/2}$ and $2p_{1/2}$ oxidation states, respectively. Further, the small peak at 166.5 eV indicates the presence of S-O bonding due to the partial oxidation of S edges in the structure [26]. Se 3d spectrum displays a doublet Se 3d spectrum and it is deconvoluted into peaks at 54.5, and 53.6 eV which are assigned to $3d_{3/2}$ and Se $3d_{5/2}$. The broad peak at 58.8 eV can arise from the Se-O bonding structure. RGO presence in $Cd_{0.6}Zn_{0.2}Ni_{0.2}S_{0.2}Se_{0.8}$ can be identified by the C 1 s and O 1 s peaks. The intensity of the C 1 s peak on the survey spectrum of RGO(0.25)-$Cd_{0.6}Zn_{0.2}Ni_{0.2}S_{0.2}Se_{0.8}$ is much higher than the one of the $Cd_{0.6}Zn_{0.2}Ni_{0.2}S_{0.2}Se_{0.8}$, which is in good correspondence with the RGO structure. The XPS spectrum of C1s is broad and asymmetric, indexing to the existence of carbon-containing species. C 1 s spectrum is deconvoluted into the peaks assigned to the C-C/C = C (285.0 eV), C-O (286.8 eV), and C = O (289.2 eV). Oxygenated functional groups of RGO are observed in the form of C = O/O = C-OH (529.7 eV), C-O (531.7 eV), $H_2O$ (533.7 eV), C-OH (536.0 eV) groups [27,28]. Table S1. gives the calculated atomic composition and atomic ratio values of $Cd_{0.6}Zn_{0.2}Ni_{0.2}S_{0.2}Se_{0.8}$ and RGO-$Cd_{0.6}Zn_{0.2}Ni_{0.2}S_{0.2}Se_{0.8}$ from XPS results. According to the data, it is verified that the atomic ratio (XPS) of $Cd_{0.6}Zn_{0.2}Ni_{0.2}S_{0.2}Se_{0.8}$ is determined as $Cd_{0.54}Zn_{0.21}Ni_{0.25}S_{0.17}Se_{0.83}$ ($Cd_xZn_yNi_{(1-x-y)}S_zSe_{(1-z)}$). When RGO-$Cd_{0.6}Zn_{0.2}Ni_{0.2}S_{0.2}Se_{0.8}$ photoelectrode is formed, there is a very slight change in the composition of $Cd_{0.6}Zn_{0.2}Ni_{0.2}S_{0.2}Se_{0.8}$, which is $Cd_{0.56}Zn_{0.25}Ni_{0.19}S_{0.21}Se_{0.79}$. In addition, the C:O ratio in RGO is 0.75:0.25.

The Raman spectra of the $Cd_{0.6}Zn_{0.2}Mo_{0.2}S_{0.2}Se_{0.8}$, $Cd_{0.6}Zn_{0.2}Ni_{0.2}S_{0.2}Se_{0.8}$, $Cd_{0.6}Zn_{0.2}Cu_{0.2}S_{0.2}Se_{0.8}$, and RGO(0.25)-$Cd_{0.6}Zn_{0.2}Ni_{0.2}S_{0.2}Se_{0.8}$ photoelectrodes excited with 532 nm of an $Ar^+$ ion laser are given in Fig. 5. The bands positioned at 177 $cm^{-1}$, 202 $cm^{-1}$, 418 $cm^{-1}$, and 615 $cm^{-1}$ belong to the Raman modes of TO (transverse optical phonon), 1LO (longitudinal optical phonon) and 2LO bands of CdZnSSe. Apart from that, the peaks at 248 $cm^{-1}$ and 404 $cm^{-1}$ correspond to the out-of-plane $A_{1g}$ vibration mode of $Cd_{0.6}Zn_0Mo_2Se_{0.8}$ [29,30]. The presence of CuSe and CuS is addressed to the peaks at around 1100 $cm^{-1}$ (antisymmetric stretching mode of CuSe) and 470 $cm^{-1}$ (S-S vibration of CuS [31,32] $A_{1g}$ Raman mode of NiSe is obvious at 202 $cm^{-1}$ since it increases the intensity of the TO peak considerably [33]. The existence of RGO formed by the reduction of GO in the composite films through electrodeposition is confirmed by the overlapping of D and G bands. In Fig.S3, the Raman spectrum of synthesized GO is explained in detail.Fig. 6.

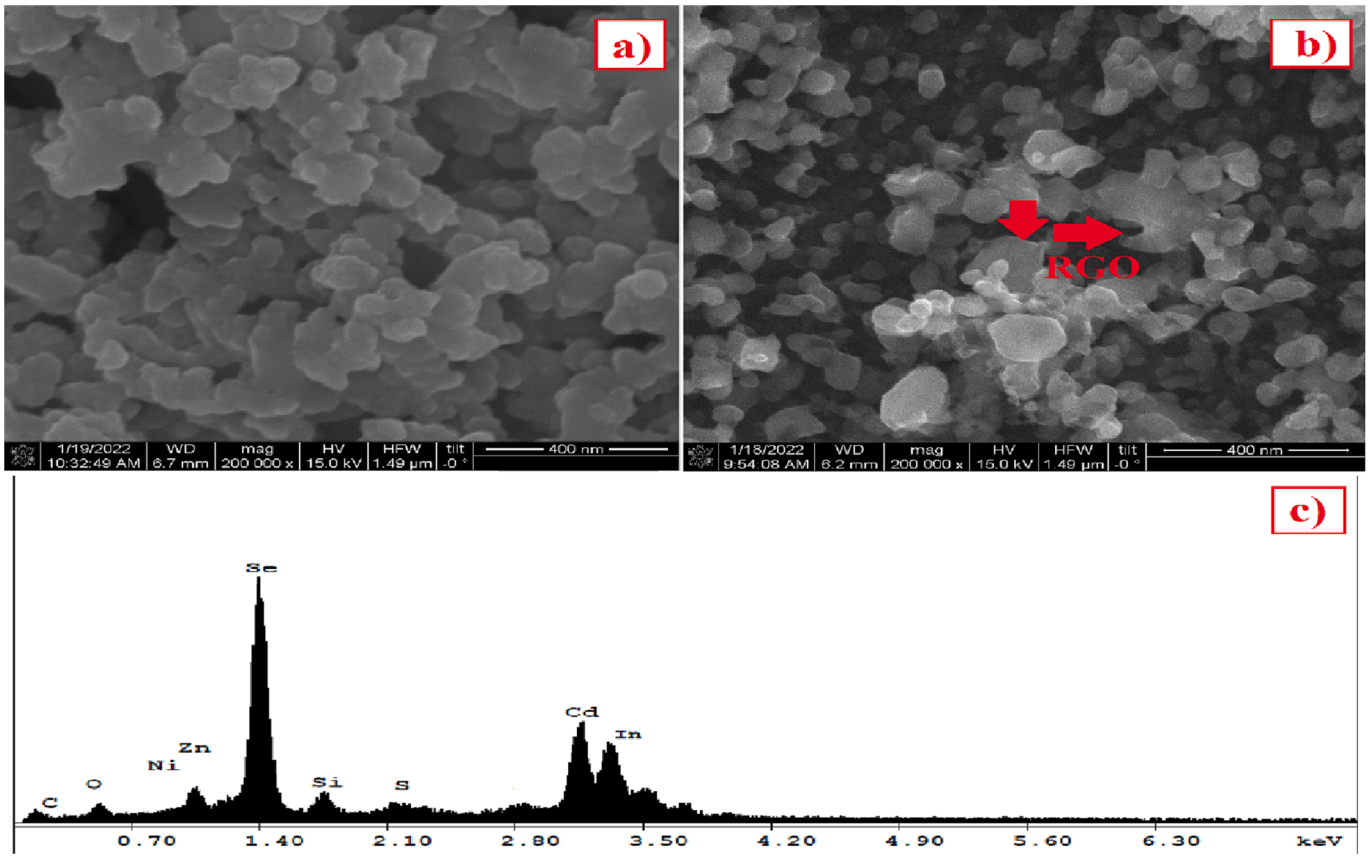


**Fig. 3.** FESEM images of the fabricated photoelectrodes at a magnification of 200000x a) $Cd_{0.6}Zn_{0.2}Ni_{0.2}S_{0.2}Se_{0.8}$, b) RGO(0.25)-$Cd_{0.6}Zn_{0.2}Ni_{0.2}S_{0.2}Se_{0.8}$, c) EDS spectra of the RGO(0.25)-$Cd_{0.6}Zn_{0.2}Ni_{0.2}S_{0.2}Se_{0.8}$.

XRD patterns are recorded to verify the structural phase confirmation of the fabricated $Cd_{0.6}Zn_{0.2}Mo_{0.2}S_{0.2}Se_{0.8}$, $Cd_{0.6}Zn_{0.2}Cu_{0.2}S_{0.2}Se_{0.8}$, $Cd_{0.6}Zn_{0.2}Ni_{0.2}S_{0.2}Se_{0.8}$, and RGO(0.25)-$Cd_{0.6}Zn_{0.2}Ni_{0.2}S_{0.2}Se_{0.8}$ composite thin films. The diffraction peaks of NiSe appear at $2\theta = 30.2°$, 33.0°, 45.4°, 50.0°, 60.2°, 62.0°, and 68.0°. This pattern is consistent with the literature [34,35]. Accordingly, the peaks at $2\theta = 30°$, 35°, 45°, and 55° represent NiS formation. The peaks located at $2\theta = 27.7°$, 30.2°, 32.3°, 41.6°, 46.0°, and 55.9° prove the existence of CuS [36]. MoS and MoSe formation are confirmed with the location of peaks at $2\theta = 33°$, 35°, 45°, and 55° [37]. Apart from that, RGO(0.25)-$Cd_{0.6}Zn_{0.2}Ni_{0.2}S_{0.2}Se_{0.8}$ exhibits a relatively broad peak between $2\theta = 20°$ and 30° diffraction angle. The reason for that might lie behind the fact that the diffraction peaks belonging to RGO overlap with other peaks [38].

The average crystallite sizes are determined according to the Debye-Scherrer equation below [39]:

$$D = (K * \lambda)/(\beta * \cos\theta) \quad (1)$$

D: average particle size (nm); K: crystallite shape factor; approximately 0.89; β:FWHM (full width at half maximum); λ: the wavelength of X-ray, θ: diffraction angle (degree).

By applying this formula, the average crystallite sizes for RGO(0.25)-$Cd_{0.6}Zn_{0.2}Ni_{0.2}S_{0.2}Se_{0.8}$ and $Cd_{0.6}Zn_{0.2}Ni_{0.2}S_{0.2}Se_{0.8}$ are calculated as 55.8 and 72.4 nm, respectively. The crystallite size becomes smaller with the presence of RGO in the structure, improving the photoelectrochemical activity via increment in the surface area [40].

Fig. 7displays the UV–vis DRS (inset) and Tauc plots of RGO(0.25)-$Cd_{0.6}Zn_{0.2}Ni_{0.2}S_{0.2}Se_{0.8}$ and $Cd_{0.6}Zn_{0.2}Ni_{0.2}S_{0.2}Se_{0.8}$ thin films which leads to finding out the optical features. The Kubelka-Munk function of the Tauc-plot method is applied to estimate the band gaps of the photoelectrodes [41].

$$(\alpha h\upsilon)^2 = A\left(h\upsilon - E_g\right) \quad (2)$$

where α, hυ, A, and $E_g$ state absorption coefficient, photon energy, proportionality constant, and band gap, respectively. The band gap values for RGO(0.25)-$Cd_{0.6}Zn_{0.2}Ni_{0.2}S_{0.2}Se_{0.8}$ and $Cd_{0.6}Zn_{0.2}Ni_{0.2}S_{0.2}Se_{0.8}$ are calculated as 1.83 and 1.84 eV, respectively. These values are almost incomparable to each other due to the relatively low concentration of RGO in RGO(0.25)-$Cd_{0.6}Zn_{0.2}Ni_{0.2}S_{0.2}Se_{0.8}$ thin film composition.

### 3.2. Photoelectrochemical performance measurements of fabricated photoelectrodes

A three-electrode system composed of an Ag/AgCl reference electrode, Pt wire counter electrode, and ITO-coated glass substrate working electrode in $Na_2S/Na_2SO_3$ sacrificial reagent is used to evaluate the photoelectrochemical activities of fabricated photoelectrodes. Linear sweep voltammetry (LSV) analyses have been performed in a potential range between −0.2 V and 1.8 V vs. RHE under chopped 1 Sun (AM 1.5G) illumination (Fig. 8) and the light is switched on and off at regular intervals during the experiment.

RHE represents the reversible hydrogen electrode (RHE) scale converted by applying the Nerst equation [42]:

$$V_{RHE} = V_{Ag/AgCl} + 0.059 \times pH + V^0_{Ag/AgCl} \quad (3)$$

where $V^0_{Ag/AgCl}$= 0.197 V and pH of the electrolyte = 13.0.

RGO(0.25)-$Cd_{0.6}Zn_{0.2}Ni_{0.2}S_{0.2}Se_{0.8}$ photoelectrode generates the highest photocurrent density at 0.8 V vs. RHE. This result can be attributed to the remarkable properties of RGO in the structure such as acting as a conductive-bridge linker, enhancing electron-hole

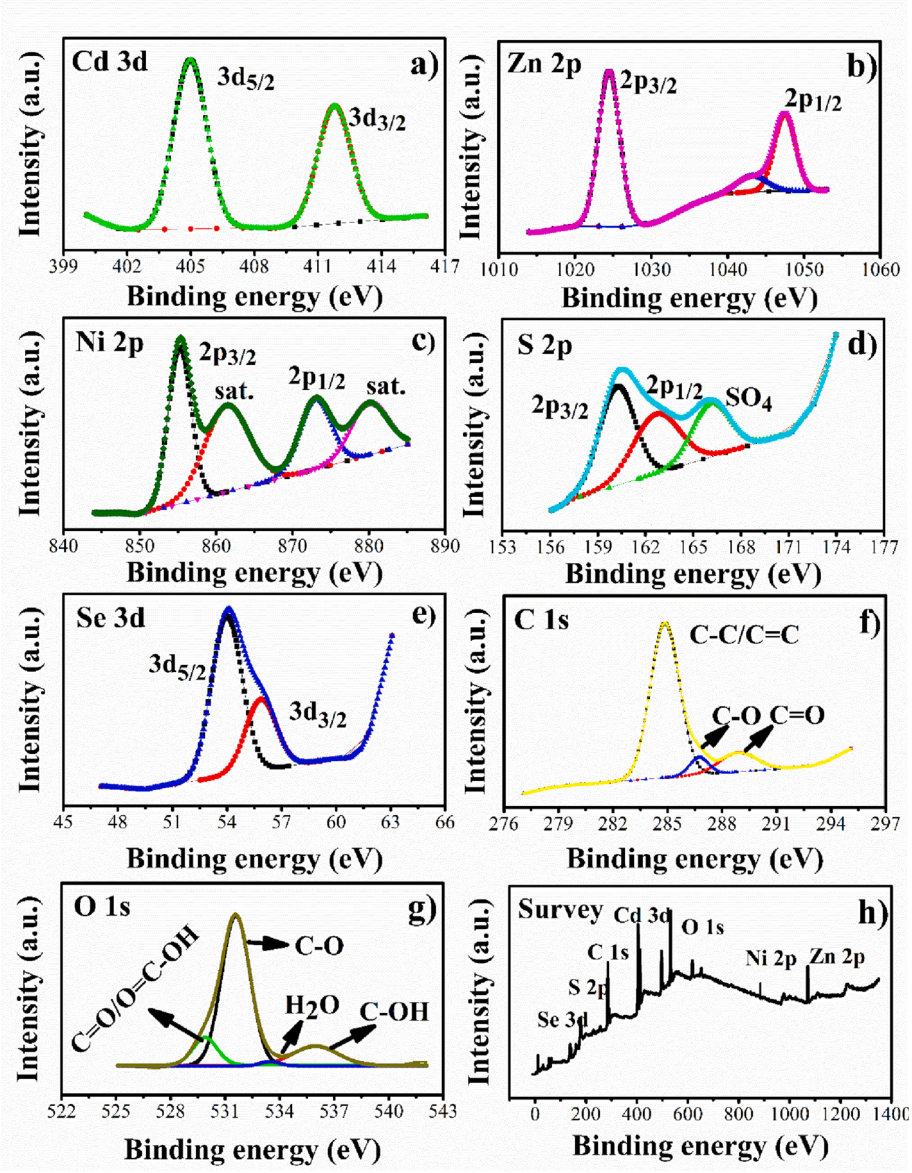


**Fig. 4.** X-ray photoelectron spectroscopy (XPS) spectra of fabricated RGO(0.25)-$Cd_{0.6}Zn_{0.2}Ni_{0.2}S_{0.2}Se_{0.8}$. a) Cd 3d, b) Zn 2p, c) Ni 2p, d) S 2p, e) Se 3d, f) C 1 s, g) O 1 s, h) Survey.

separation, and increasing in photocurrent [43] which is verified by several reported studies in the literature [44–47]. In comparison, $Cd_{0.6}Zn_{0.2}Ni_{0.2}S_{0.2}Se_{0.8}$ photoelectrode yields close, yet apparently lower photocurrent density. In terms of LSV, the performances of $Cd_{0.6}Zn_{0.2}Cu_{0.2}S_{0.2}Se_{0.8}$ and $Cd_{0.6}Zn_{0.2}Mo_{0.2}S_{0.2}Se_{0.8}$ photoelectrodes come after $Cd_{0.6}Zn_{0.2}Ni_{0.2}S_{0.2}Se_{0.8}$ photoelectrode. In the LSV curves, the increasing dark currents are observed as the applied voltage increases, which might appear owing to the leakage of charge carriers near an electrode surface into the electrolyte [48].

Fig. 9 shows the chronoamperometry results measured at 0.8 V bias (vs. RHE) for all the above-investigated photoelectrodes for six light on-light off cycles at 50 s intervals. According to Fig. 9.a, it can be deduced that all photoelectrodes exhibit n-type conductivity characteristics during repetitive on-off illumination cycles. Moreover, RGO(0.25)-$Cd_{0.6}Zn_{0.2}Ni_{0.2}S_{0.2}Se_{0.8}$ photoelectrode displays more efficient separation of photogenerated charge carriers and relatively lower photocorrosion, achieving the highest photocurrent density of 5.34 mA $cm^{-2}$. The photocurrent density of RGO(0.25)-$Cd_{0.6}Zn_{0.2}Ni_{0.2}S_{0.2}Se_{0.8}$ is followed by $Cd_{0.6}Zn_{0.2}Ni_{0.2}S_{0.2}Se_{0.8}$, $Cd_{0.6}Zn_{0.2}Cu_{0.2}S_{0.2}Se_{0.8}$, and $Cd_{0.6}Zn_{0.2}Mo_{0.2}S_{0.2}Se_{0.8}$ photoelectrodes, which corresponds to 5.08, 3.16, and 2.53 mA $cm^{-2}$, respectively. Fig. 9b shows the long-term stability measurement of RGO-$Cd_{0.6}Zn_{0.2}Ni_{0.2}S_{0.2}Se_{0.8}$ photoelectrode under the continuous simulated sunlight illumination at 0.8 V vs. RHE by chronoamperometry technique. According to Fig. 9b, the photocurrent density has decreased in time due to decreasing in the concentration of the sacrificial reagent as well as a slight decrease in the electrode stability. At the end of 2nd hour, 73.1% of its initial photocurrent density remained.

Mott-Schottky (M−S) analysis is performed to determine the flat band potentials ($V_{fb}$) and charge carrier density values ($N_D$) of RGO (0.25)-$Cd_{0.6}Zn_{0.2}Ni_{0.2}S_{0.2}Se_{0.8}$, $Cd_{0.6}Zn_{0.2}Ni_{0.2}S_{0.2}Se_{0.8}$, $Cd_{0.6}Zn_{0.2}Cu_{0.2}S_{0.2}Se_{0.8}$, and $Cd_{0.6}Zn_{0.2}Mo_{0.2}S_{0.2}Se_{0.8}$ photoelectrodes. Practically, above the flat band potential the photoresponse can be initiated [49]. M−S plots have been collected at a frequency of 100 Hz under dark conditions. Fig. 10 demonstrates the M−S plots for RGO(0.25)-$Cd_{0.6}Zn_{0.2}Ni_{0.2}S_{0.2}Se_{0.8}$, $Cd_{0.6}Zn_{0.2}Ni_{0.2}S_{0.2}Se_{0.8}$, $Cd_{0.6}Zn_{0.2}Cu_{0.2}S_{0.2}Se_{0.8}$, and $Cd_{0.6}Zn_{0.2}Mo_{0.2}S_{0.2}Se_{0.8}$ photoelectrodes. The positive slopes of photoelectrodes suggest n-type conductivity behavior which is compatible with LSV experiments and the flat band potential values are obtained from the intercept of the linear part of M−S plots. According to

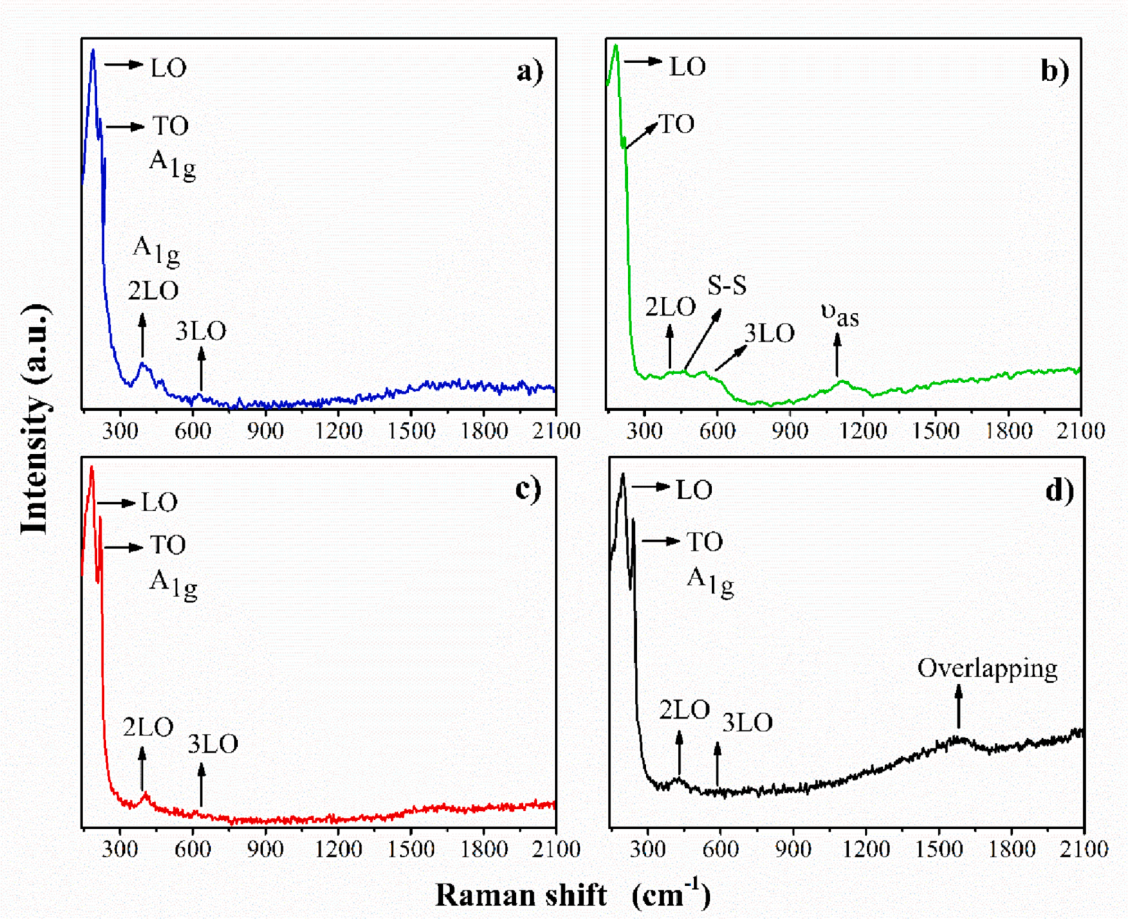


**Fig. 5.** Raman spectra of composite thin films a) $Cd_{0.6}Zn_{0.2}Mo_{0.2}S_{0.2}Se_{0.8}$, b) $Cd_{0.6}Zn_{0.2}Cu_{0.2}S_{0.2}Se_{0.8}$, c) $Cd_{0.6}Zn_{0.2}Ni_{0.2}S_{0.2}Se_{0.8}$, d) RGO(0.25)-$Cd_{0.6}Zn_{0.2}Ni_{0.2}S_{0.2}Se_{0.8}$.

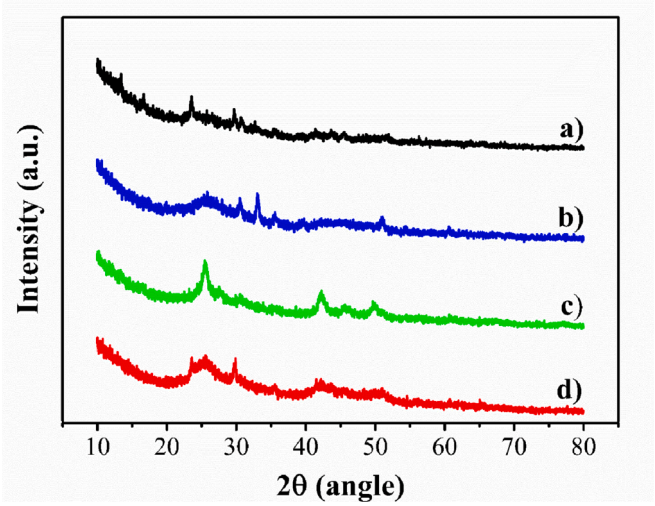


**Fig. 6.** XRD patterns of prepared thin films a) RGO(0.25)-$Cd_{0.6}Zn_{0.2}Ni_{0.2}S_{0.2}Se_{0.8}$, b) $Cd_{0.6}Zn_{0.2}Mo_{0.2}S_{0.2}Se_{0.8}$, c) $Cd_{0.6}Zn_{0.2}Cu_{0.2}S_{0.2}Se_{0.8}$, d) $Cd_{0.6}Zn_{0.2}Ni_{0.2}S_{0.2}Se_{0.8}$.

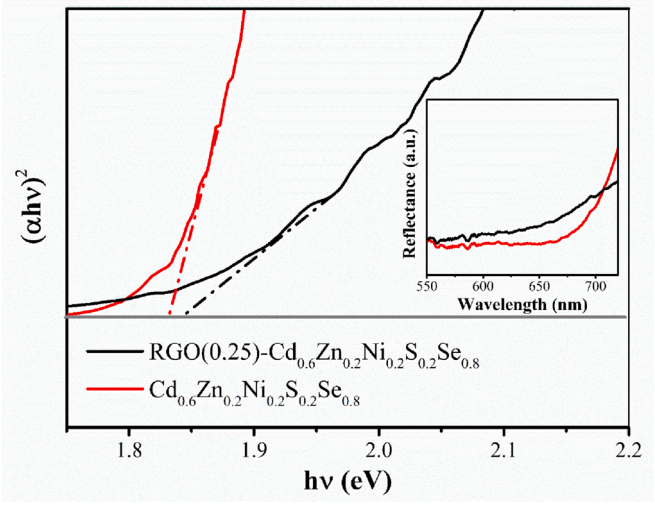


**Fig. 7.** UV–vis DRS (inset) and Tauc plots of RGO(0.25)-$Cd_{0.6}Zn_{0.2}Ni_{0.2}S_{0.2}Se_{0.8}$ and $Cd_{0.6}Zn_{0.2}Ni_{0.2}S_{0.2}Se_{0.8}$ thin films.

the Fig. 10, the flat band potentials of RGO(0.25)-$Cd_{0.6}Zn_{0.2}Ni_{0.2}S_{0.2}Se_{0.8}$, $Cd_{0.6}Zn_{0.2}Ni_{0.2}S_{0.2}Se_{0.8}$, $Cd_{0.6}Zn_{0.2}Cu_{0.2}S_{0.2}Se_{0.8}$ and $Cd_{0.6}Zn_{0.2}Mo_{0.2}S_{0.2}Se_{0.8}$ photoelectrodes are estimated as −0.24, −0.18, −0.05 and 0.02 V vs. RHE. Yet, LSV results suggest that the onset potentials are shifted to a more positive side, which designates the lack of an efficient electron-hole extracting mechanism. Therefore, an external bias is necessary to initiate photoresponse. However, this external bias is relatively low for RGO(0.25)-$Cd_{0.6}Zn_{0.2}Ni_{0.2}S_{0.2}Se_{0.8}$ photoelectrode, which is in good agreement with previous results. Fig. 10.

The slope of the M−S plot is inversely proportional to the $N_D$ value of

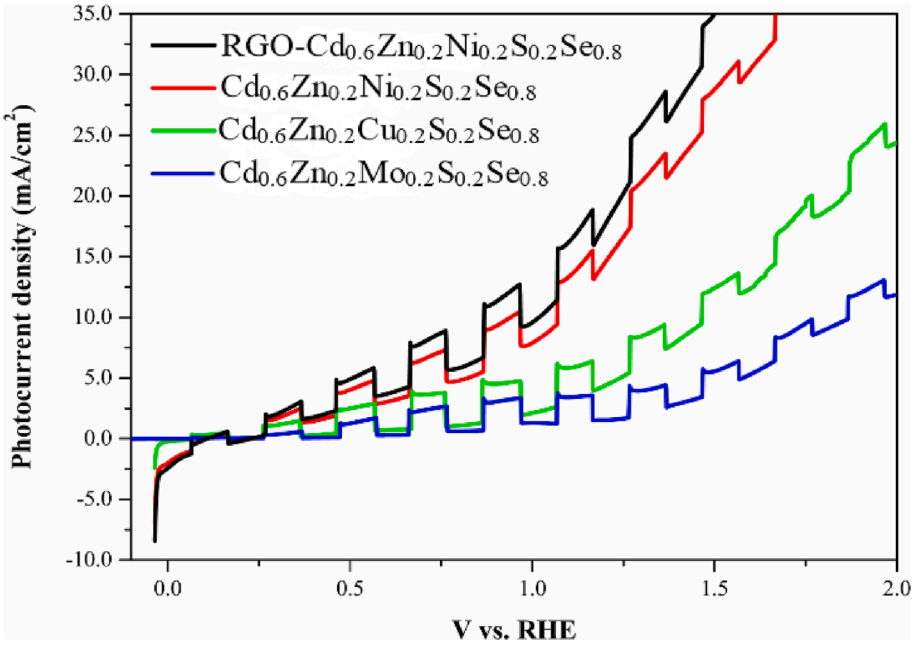


**Fig. 8.** LSV curves of $Cd_{0.6}Zn_{0.2}Mo_{0.2}S_{0.2}Se_{0.8}$, $Cd_{0.6}Zn_{0.2}Cu_{0.2}S_{0.2}Se_{0.8}$, $Cd_{0.6}Zn_{0.2}Ni_{0.2}S_{0.2}Se_{0.8}$ and RGO(0.25)- $Cd_{0.6}Zn_{0.2}Ni_{0.2}S_{0.2}Se_{0.8}$ photoelectrodes.

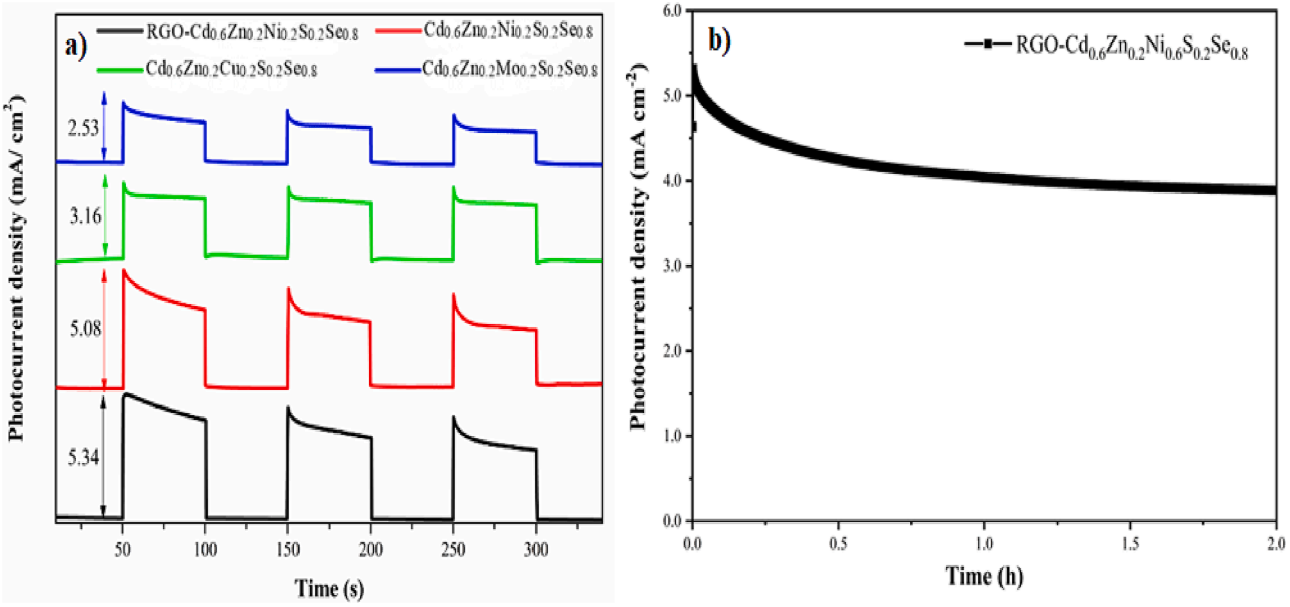


**Fig. 9.** A) chronoamperometric (ca) curves of $cd_{0.6}Zn_{0.2}Mo_{0.2}S_{0.2}Se_{0.8}$, $Cd_{0.6}Zn_{0.2}Cu_{0.2}S_{0.2}Se_{0.8}$, $Cd_{0.6}Zn_{0.2}Ni_{0.2}S_{0.2}Se_{0.8}$ and RGO(0.25)-$Cd_{0.6}Zn_{0.2}Ni_{0.2}S_{0.2}Se_{0.8}$ photoelectrodes. b) Long-term stability measurement of RGO(0.25)- $Cd_{0.6}Zn_{0.2}Ni_{0.2}S_{0.2}Se_{0.8}$ photoelectrode under the continuous simulated sunlight illumination at 0.8 V vs. RHE.

a photoelectrode [50]. Indeed, the slope of the M−S curve of RGO(0.25)-$Cd_{0.6}Zn_{0.2}Ni_{0.2}S_{0.2}Se_{0.8}$ is the lowest.

Charge carrier density values of photoelectrodes are calculated based on Eq (4):

$$1/C^2 = \left(2/\varepsilon 0 \varepsilon e N A^2\right)\left(V - V_{fb} - KT/e\right) \quad (4)$$

C: capacitance of space charge region, e: electron charge ($1.603\times10^{-19}$C), K: Boltzmann constant ($1.38\times10^{-23}$ J/K), T: absolute temperature (K), ε:dielectric constant of semiconductor, $\varepsilon_0$: permittivity of vacuum ($8.854\times10^{-12}$F $m^{-1}$), $N_D$: charge carrier density, A: area of the photoelectrode, V: applied potential, $V_{fb}$: flat band potential. (KT/e is neglected at room temperature under 1 atm pressure).

The charge carrier density values ($N_D$) of all fabricated photoelectrodes derived from M−S plots are summarized in Table S2. Among all these photoelectrodes, RGO(0.25)-$Cd_{0.6}Zn_{0.2}Ni_{0.2}S_{0.2}Se_{0.8}$ has the highest charge carrier density of $4.88\times10^{18}$ which mainly attributes to its admirable charge transfer properties of the photogenerated electron-hole pairs.

To further investigate the charge transfer and kinetics, electrochemical impedance spectroscopy (EIS) has been recorded (Fig. 11). EIS measurements are employed in the frequency range of $10^5$ to $10^{-2}$ Hz under dark conditions. The Nyquist plots suggest that the photoelectrodes exhibit similar solution resistance, but quite different charge transport resistance shown in Fig. 11a and b. The charge transfer resistance of $Cd_{0.6}Zn_{0.2}Ni_{0.2}S_{0.2}Se_{0.8}$ has decreased significantly upon

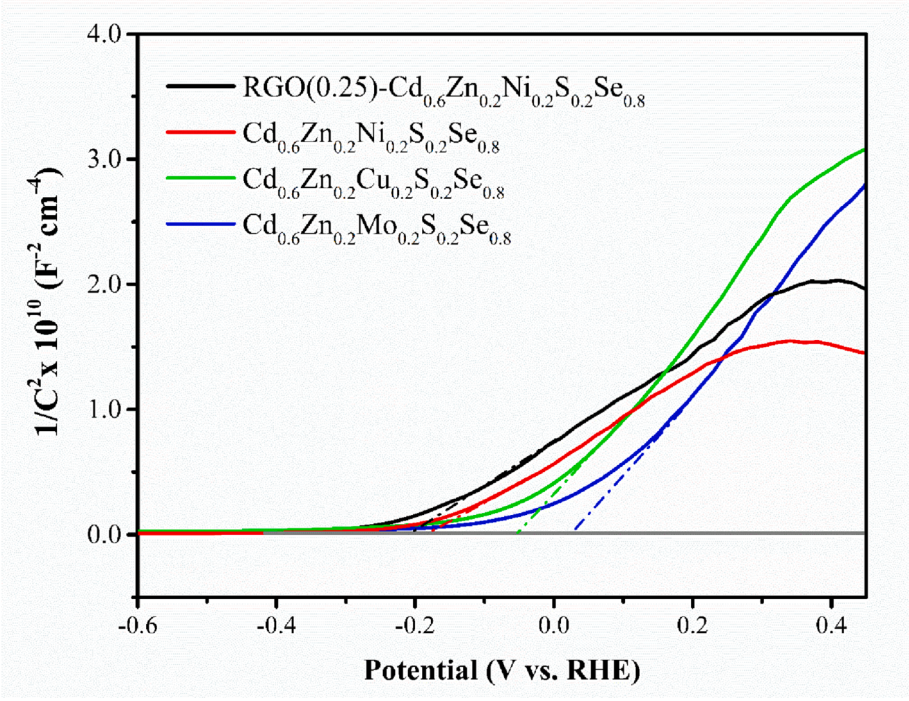


**Fig. 10.** M−S plots of for RGO(0.25)-$Cd_{0.6}Zn_{0.2}Ni_{0.2}S_{0.2}Se_{0.8}$, $Cd_{0.6}Zn_{0.2}Ni_{0.2}S_{0.2}Se_{0.8}$, $Cd_{0.6}Zn_{0.2}Cu_{0.2}S_{0.2}Se_{0.8}$ and $Cd_{0.6}Zn_{0.2}Mo_{0.2}S_{0.2}Se_{0.8}$ photoelectrodes.

including RGO in photoelectrode composition and charge transfer at the semiconductor-electrolyte interface is promoted. On the contrary, the behavior of the Nyquist plot for $Cd_{0.6}Zn_{0.2}Mo_{0.2}S_{0.2}Se_{0.8}$ photoelectrode can be responsible for the low photocurrent density. Nyquist curves are fitted using an equivalent Randles circuit model with a Warburg element as given in Fig. 11c. This model includes the elements of the solution resistance (Rs), the Warburg impedance (W), charge transfer resistance ($R_{ct}$), and the constant phase element (CPE). Here, Rs is the series resistance associated with ITO, sacrificial electrolyte, and external contact for the electrochemical device. $R_{ct}$ states the charge transfer resistance between the semiconductor and electrolyte interface. CPE accounts for the capacitance due to the formation of a double layer in the photoelectrode. The adopted EIS fitting model yields $R_s$ and $R_{ct}$ values for RGO(0.25)- $Cd_{0.6}Zn_{0.2}Ni_{0.2}S_{0.2}Se_{0.8}$, $Cd_{0.6}Zn_{0.2}Ni_{0.2}S_{0.2}Se_{0.8}$, $Cd_{0.6}Zn_{0.2}Mo_{0.2}S_{0.2}Se_{0.8}$ and $Cd_{0.6}Zn_{0.2}Cu_{0.2}S_{0.2}Se_{0.8}$ as 16.40 and 223.9 Ω $cm^{-2}$, 26.02 and 245.3 Ω $cm^{-2}$, 34.27 and 998.5 Ω $cm^{-2}$, 11.70 and 647.7 Ω $cm^{-2}$, respectively. Therefore, the lowest Rs and $R_{ct}$ values of RGO(0.25)-$Cd_{0.6}Zn_{0.2}Ni_{0.2}S_{0.2}Se_{0.8}$ can be attributed to high photoelectrochemical properties which are proven with the chronoamperometry experiments. The other determined EIS parameter values achieved from the data fitting are listed in Table S3.

Applied bias photon to current conversion efficiency (ABPE) which plays an important role in characterizing the PEC system is estimated based on Eq (5) and demonstrated in Fig. 12 [50,51]:

$$ABPE = J_{ph}\ (V_{redox} - V_{bias})/P_{bias} \quad (5)$$

where $J_{ph}$ depicts the photocurrent density (mA $cm^{-2}$), $V_{redox}$ is 0.936 V. $V_{bias}$ states the applied bias potential, and $P_{bias}$ corresponds to the light intensity under 1 sun of AM1.5G illumination (100 mW $cm^{-2}$). For the $H_2$ evolution on CB and $Na_2S/Na_2SO_3$ oxidation on the VB, the overall potential should be 0.936 V. As reported in the literature, The scavenging of holes by the sacrificial agents generally depends upon their oxidation potential and the reported oxidation potential of the sodium sulfide/sulfite is 0.936 eV which plays an important role in the photocatalytic water-splitting reaction [52]. As expected, the maximum ABPE values for $Cd_{0.6}Zn_{0.2}Ni_{0.2}S_{0.2}Se_{0.8}$ and RGO(0.25)-$Cd_{0.6}Zn_{0.2}Ni_{0.2}S_{0.2}Se_{0.8}$ photoelectrodes are determined as 1.43% and 1.95%, respectively.

Faradaic efficiency is also significant for the evaluation of a PEC system and is determined by using the following equation [53]:

$$FE\% = (2F \times n_i/(I \times t)) \times 100 \quad (6)$$

where $n_i$ represents $H_2$ mole number (mol), I and t state current (A) and time (s), and F is the Faraday's constant (96485C $mol^{-1}$).

The experimental $H_2$ production rate determined by gas chromatography for RGO(0.25)-$Cd_{0.6}Zn_{0.2}Ni_{0.2}S_{0.2}Se_{0.8}$ photoelectrode is found as 88.5 μmol $h^{-1}$. By applying Eq.6, the FE% value is calculated as 88.8% for RGO(0.25)-$Cd_{0.6}Zn_{0.2}Ni_{0.2}S_{0.2}Se_{0.8}$ which exhibits the best photoelectrochemical performance. As a result, this photoelectrode has promising potential for photoelectrochemical hydrogen production applications.

## 4. Conclusion

This report successfully presents the fabrication of CdZnMSSe (M: Ni, Cu, Mo) and RGO-CdZnNiSSe composite films for photoelectrochemical hydrogen production applications through one-step electrodeposition at room temperature by using the three-electrode system. The photoelectrochemical performance of photoelectrodes is investigated in an aqueous electrolyte composed of 0.25 mol $dm^{-3}$ $Na_2S$ and 0.35 mol $dm^{-3}$ $Na_2SO_3$. $Cd_{0.6}Zn_{0.2}Ni_{0.2}S_{0.2}Se_{0.8}$ and RGO(0.25)-$Cd_{0.6}Zn_{0.2}Ni_{0.2}S_{0.2}Se_{0.8}$ photoelectrodes possess enhanced photocurrent densities of 5.08 mA $cm^{-2}$ and 5.34 mA $cm^{-2}$ at 0.8 V vs RHE respectively. Based on the findings, the presence of RGO in the composite films which leads to effective separation of charge carriers and prevents the recombination of photogenerated electron-hole pairs improves the photoelectrochemical activity. Furthermore, the ABPE values of $Cd_{0.6}Zn_{0.2}Ni_{0.2}S_{0.2}Se_{0.8}$ and RGO(0.25)-$Cd_{0.6}Zn_{0.2}Ni_{0.2}S_{0.2}Se_{0.8}$ reach 1.43% and 1.95%, respectively. As a result, this study provides a profound impact to prepare photoanode with highly efficient, inexpensive, and stable properties by using facile one-step electrodeposition for photoelectrochemical hydrogen production.

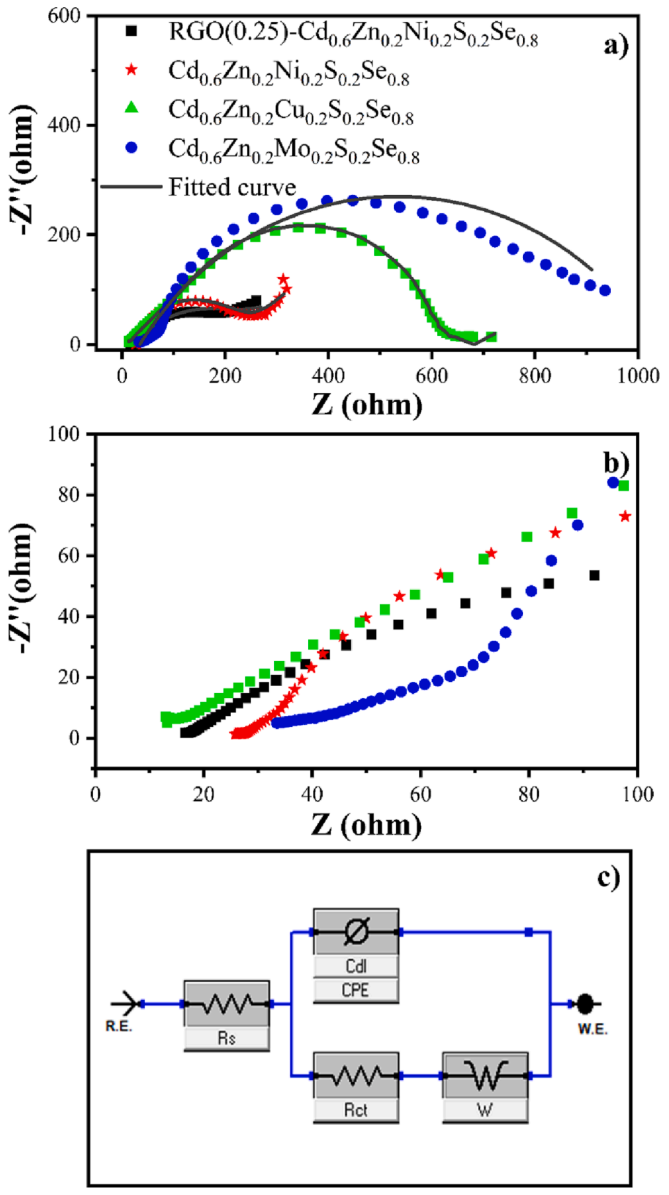


**Fig. 11.** A) Nyquist plots and fitted curves, b) The enlarged view of nyquist plots of $Cd_{0.6}Zn_{0.2}Mo_{0.2}S_{0.2}Se_{0.8}$, $Cd_{0.6}Zn_{0.2}Cu_{0.2}S_{0.2}Se_{0.8}$, $Cd_{0.6}Zn_{0.2}Ni_{0.2}S_{0.2}Se_{0.8}$ and RGO(0.25)-$Cd_{0.6}Zn_{0.2}Ni_{0.2}S_{0.2}Se_{0.8}$ photoelectrodes, c) Equivalent circuit model used for EIS data fitting (R.E.: Reference electrode, W.E: Working electrode, $R_s$: Series resistance, $R_{ct}$: Charge transfer resistance, CPE: Constant phase element, W: Finite-length Warburg element).

## CRediT authorship contribution statement

**Özlem Uğuz Neli:** Writing – original draft, Methodology, Investigation, Data curation, Conceptualization. **Özlem Budak:** Writing – original draft, Methodology, Investigation, Data curation, Conceptualization. **Fatma Karaca:** Writing – review & editing, Supervision. **Bahadır Keskin:** Visualization, Conceptualization. **Ali Rıza Özkaya:** Writing – review & editing, Validation. **Atıf Koca:** Writing – review & editing, Validation, Supervision, Resources, Conceptualization.

## Declaration of Competing Interest

The authors declare that they have no known competing financial interests or personal relationships that could have appeared to influence the work reported in this paper.

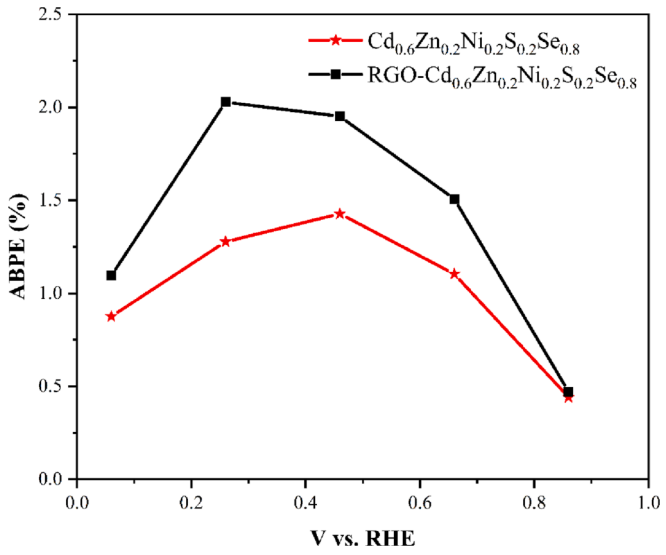


**Fig. 12.** ABPE values for $Cd_{0.6}Zn_{0.2}Ni_{0.2}S_{0.2}Se_{0.8}$ and RGO(0.25)-$Cd_{0.6}Zn_{0.2}Ni_{0.2}S_{0.2}Se_{0.8}$ photoelectrodes.

## Data availability

No data was used for the research described in the article.

## Acknowledgments

This work was supported by The Scientific and Technological Research Council of Turkey (TUBITAK) [Grant Number: 219M328] and the Scientific Research Projects Commission (BAPKO) of Marmara University [Grant Number: FDK-2020-10022]. Atıf Koca also thanks the Turkish Academy of Sciences (TÜBA) for the financial support.

## Appendix A. Supplementary data

Supplementary data to this article can be found online at https://doi.org/10.1016/j.jphotochem.2023.114657.

## References

[1] Q. Shen, et al., Photoelectrocatalytic hydrogen production of heterogeneous photoelectrodes with different system configurations of CdSe nanoparticles, Au nanocrystals and TiO2 nanotube arrays, International Journal of Hydrogen Energy 45 (51) (2020) 26688–26700.
[2] P. Peerakiatkhajohn, et al., Bifunctional photoelectrochemical process for humic acid degradation and hydrogen production using multi-layered p-type Cu2O photoelectrodes with plasmonic Au@ TiO2, Journal of Hazardous Materials 402 (2021), 123533.
[3] X. Sun, et al., Beyond Photosynthesis: H2O/H2O2/O2 Self-Circulation-Based Biohybrid Photoelectrochemical Cells for Direct and Sustainable Solar-to-Fuel-to-Electric Power Conversion, Journal of the American Chemical Society (2022).
[4] G.O. Rabell, M.A. Cruz, I. Juárez-Ramírez, Photoelectrochemical (PEC) analysis of ZnO/Al photoelectrodes and its photocatalytic activity for hydrogen production, International Journal of Hydrogen Energy (2022).
[5] M. Ben-Naim, et al., Demonstration of photoreactor platform for on-sun unassisted photoelectrochemical hydrogen generation with tandem III–V photoelectrodes, Chem Catalysis 2 (1) (2022) 195–209.
[6] Y. Choi, et al., In situ measurement of photostability of CdSe/CdS/ZnO nanowires photoelectrode for photoelectrochemical water splitting, Sensors and Actuators B: Chemical 221 (2015) 113–119.
[7] N.D. Quang, et al., Optimization strategy for CdSe@ CdS core–shell nanorod structures toward high performance water splitting photoelectrodes, Materials Research Bulletin 129 (2020), 110914.
[8] L. Jiang, et al., Graphene-Sb2Se3 thin films photoelectrode synthesized by in situ electrodeposition, Materials Letters 224 (2018) 109–112.
[9] F. Ghasemi, M.H. Amiri, Facile in situ fabrication of rGO/MoS2 heterostructure decorated with gold nanoparticles with enhanced photoelectrochemical performance, Applied Surface Science 570 (2021), 151228.
[10] Q. Shen, et al., The dual effects of RGO films in TiO2/CdSe heterojunction: Enhancing photocatalytic activity and improving photocorrosion resistance, Applied Surface Science 481 (2019) 1515–1523.

[11] M. Tokay, A.A. Oladipo, M. Kusaf, Octahedral-like, Ni0., 3Zn0. 7Fe2O4–TiO2 nanohybrid material as photoanode of natural dye-sensitized solar cells, Optical Materials 128 (2022), 112407.
[12] G. Zhang, et al., ThCr2Si2-type quaternary chalcogenides as efficient Pt-free counter electrodes for dye-sensitized solar cells, Journal of Alloys and Compounds 817 (2020), 152797.
[13] Q. Sun, L. Qi, Triple-layer ITO/BiVO4/Fe2TiO5 heterojunction photoanode coated with iron silicate for highly efficient solar water splitting, Chemical Engineering Journal 426 (2021), 131290.
[14] L. Zhou, et al., Quaternary oxide photoanode discovery improves the spectral response and photovoltage of copper vanadates, Matter 3 (5) (2020) 1614–1630.
[15] M. Tanaka, et al., Photocatalytic water splitting on the CuInS2 photoelectrodes: Effects of co-electrodeposition mechanisms on the photoelectrochemical properties, Catalysis Today (2022).
[16] A.K. Ayal, et al., Sensitization of TiO2 nanotube arrays photoelectrode via homogeneous distribution of CdSe nanoparticles by electrodeposition techniques, Journal of Physics and Chemistry of Solids 153 (2021), 110006.
[17] Ö. Uğuz, Ö. Budak, A. Koca, Simultaneous electrodeposition of electrochemically reduced graphene oxide-binary metal chalcogenide composites to enhance photoelectrochemical performance, International Journal of Hydrogen Energy 46 (71) (2021) 35290–35301.
[18] M. Cao, et al., Enhanced photoelectrochemical water splitting with template-free electrodeposition of SnS nanorods photoelectrode, Journal of Alloys and Compounds 830 (2020), 154729.
[19] S.M. Ho, Metal chalcogenide thin films for photoelectrochemical cell applications: a review, Middle-East Journal of Scientific Research 24 (4) (2016) 1232–1235.
[20] K. Zarębska, T. Łęcki, M. Skompska, Synthesis of CdSe on FTO-supported ZnO nanorods by SILAR and electrochemical methods and comparison of photoelectrochemical properties of FTO/ZnO/CdSe systems in aqueous S2−/Sn2− electrolyte, Journal of Electroanalytical Chemistry 819 (2018) 459–468.
[21] D.C. Marcano, et al., Improved synthesis of graphene oxide, ACS nano 4 (8) (2010) 4806–4814.
[22] J. Su, et al., On the role of metal atom doping in hematite for improved photoelectrochemical properties: a comparison study, RSC advances 6 (104) (2016) 101745–101751.
[23] S. Kumar, S. Ahirwar, A.K. Satpati, Insight into the PEC and interfacial charge transfer kinetics at the Mo doped BiVO 4 photoanodes, RSC advances 9 (70) (2019) 41368–41382.
[24] Z. Yan, L. Du, D.L. Phillips, Multilayer core–shell MoS 2/CdS nanorods with very high photocatalytic activity for hydrogen production under visible-light excitation and investigation of the photocatalytic mechanism by femtosecond transient absorption spectroscopy, RSC advances 7 (88) (2017) 55993–55999.
[25] H. Huang, et al., Conductive metal–organic frameworks with extra metallic sites as an efficient electrocatalyst for the hydrogen evolution reaction, Advanced Science 7 (9) (2020) 2000012.
[26] B. Li, et al., Preparation of monolayer MoS2 quantum dots using temporally shaped femtosecond laser ablation of bulk MoS2 targets in water, Scientific Reports 7 (1) (2017) 1–12.
[27] H. Nie, et al., Excellent tribological properties of lower reduced graphene oxide content copper composite by using a one-step reduction molecular-level mixing process, Materials 11 (4) (2018) 600.
[28] V.R. Moreira, et al., Graphene oxide in the remediation of norfloxacin from aqueous matrix: simultaneous adsorption and degradation process, Environmental Science and Pollution Research 27 (27) (2020) 34513–34528.
[29] K. Anuar, et al., Cathodic electrodeposition of Cu2S thin film for solar energy conversion, Solar energy materials and solar cells 73 (4) (2002) 351–365.
[30] R. Levinas, N. Tsyntsaru, H. Cesiulis, The characterisation of electrodeposited MoS2 thin films on a foam-based electrode for hydrogen evolution, Catalysts 10 (10) (2020) 1182.
[31] T. Yang, et al., Excitation mechanism of A 1g mode and origin of nonlinear temperature dependence of Raman shift of CVD-grown mono-and few-layer MoS 2 films, Optics express 24 (11) (2016) 12281–12292.
[32] P. Tonndorf, et al., Photoluminescence emission and Raman response of monolayer MoS 2, MoSe 2, and WSe 2, Optics express 21 (4) (2013) 4908–4916.
[33] B.J. Rani, et al., Investigation on copper based oxide, sulfide and selenide derivatives oxygen evolution reaction activity, Applied Nanoscience 10 (11) (2020) 4299–4306.
[34] Z. Zou, et al., An Fe-doped nickel selenide nanorod/nanosheet hierarchical array for efficient overall water splitting, Journal of Materials Chemistry A 7 (5) (2019) 2233–2241.
[35] R. Karthikeyan, et al., Single-step synthesis and catalytic activity of structure-controlled nickel sulfide nanoparticles, CrystEngComm 17 (29) (2015) 5431–5439.
[36] M. Jing, et al., Dataset analysis on Cu9S5 material structure and its electrochemical behavior as anode for sodium-ion batteries, Data in brief 20 (2018) 790–793.
[37] L. Su, Y. Xiao, G. Han, Synthesis of highly active cobalt molybdenum sulfide nanosheets by a one-step hydrothermal method for use in dye-sensitized solar cells, Journal of Materials Science 52 (23) (2017) 13541–13551.
[38] L. Zhang, et al., Hydrothermal synthesis of N-doped RGO/MoSe2 composites and enhanced electro-catalytic hydrogen evolution, Journal of Materials Science 52 (23) (2017) 13561–13571.
[39] M. Hussein, A.,, et al., Steps toward the band gap identification in polystyrene based solid polymer nanocomposites integrated with tin titanate nanoparticles, Polymers 12 (10) (2020) 2320.
[40] M.-S. Liang, et al., Studies on the effects of crystallite sizes and scattering layers on the conversion efficiency of dye-sensitized solar cell, Journal of Power and Energy Engineering 2 (12) (2014) 18.
[41] G.D. Gesesse, et al., On the analysis of diffuse reflectance measurements to estimate the optical properties of amorphous porous carbons and semiconductor/carbon catalysts, Journal of Photochemistry and Photobiology A: Chemistry 398 (2020), 112622.
[42] Y. Hou, et al., Porosity-enhanced solar powered hydrogen generation in GaN photoelectrodes, Applied Physics Letters 111 (20) (2017), 203901.
[43] X. Zhang, et al., Fabrication of WO3/RGO/Ni: FeOOH heterostructure for synergistically enhancing photoelectrochemical water oxidation, Applied Surface Science 542 (2021), 148579.
[44] B. Li, et al., Construction of metal/WO2. 72/rGO ternary nanocomposites with optimized adsorption, photocatalytic and photoelectrochemical properties, Applied Catalysis B: Environmental 198 (2016) 325–333.
[45] Q. Shi, et al., Enriched photoelectrochemical performance of phosphate doped BiVO4 photoelectrode by coupling FeOOH and rGO, Journal of The Electrochemical Society 165 (4) (2017) H3018.
[46] M. Nasiri, et al., Elevated temperature annealed α-Fe2O3/reduced graphene oxide nanocomposite photoanode for photoelectrochemical water oxidation, J Environ Chem Eng 7 (2) (2019), 102999.
[47] R. Ranjan, M. Kumar, A. Sinha, Development and characterization of rGO supported CdSMoS2 photoelectrochemical catalyst for splitting water by visible light, International Journal of Hydrogen Energy 44 (31) (2019) 16176–16189.
[48] C. Jia, et al., Enhanced photoelectrochemical performance of black Si electrode by forming a pn junction, Journal of Materials Science: Materials in Electronics 29 (24) (2018) 20734–20741.
[49] A. Deshpande, et al., Orthorhombic/cubic Cd 2 SnO 4 nanojunctions: enhancing solar water splitting efficiency by the suppression of charge recombination, Journal of Materials Chemistry A 2 (2) (2014) 492–499.
[50] H. Zhao, et al., Engineering the Interfacial Structure of Heavy Metal-Free Colloidal Heterostructured Quantum Dots for High-Efficiency Photoelectrochemical Water Oxidation without Co-Catalyst, Advanced Energy and Sustainability Research (2022) 2200142.
[51] C. Jiang, et al., Photoelectrochemical devices for solar water splitting–materials and challenges, Chemical Society Reviews 46 (15) (2017) 4645–4660.
[52] A. Mehtab, S.M. Alshehri, T. Ahmad, Photocatalytic and photoelectrocatalytic water splitting by porous g-C3N4 nanosheets for hydrogen generation, ACS Applied Nano Materials 5 (9) (2022) 12656–12665.
[53] W. Ma, et al., Nickel and indium core-shell co-catalysts loaded silicon nanowire arrays for efficient photoelectrocatalytic reduction of CO2 to formate, Journal of Energy Chemistry 54 (2021) 422–428.